# Size distribution and mixing state of black carbon particles during a heavy air pollution episode in Shanghai

Xianda Gong[1], Ci Zhang[1], Hong Chen[1], Sergey A. Nizkorodov[2], Jianmin Chen[1,3], Xin Yang[1,3*]

1 Shanghai Key Laboratory of Atmospheric Particle Pollution and Prevention, Department of Environmental Science and Engineering, Fudan University, Shanghai 200433, China

2 Department of Chemistry, University of California, Irvine, California 92697, United States

3 Fudan-Tyndall Center, Fudan University, Shanghai 200433, China

Correspondence to: Xin Yang (yangxin@fudan.edu.cn)

**Abstract:** A Single Particle Aerosol Mass Spectrometer (SPAMS), a Single Particle Soot Photometer (SP2) and various meteorological instruments were employed to investigate the chemical and physical properties of black carbon (BC) aerosols during a regional air pollution episode in urban Shanghai over a five-day period in December 2013. The refractory black carbon (rBC) mass concentrations measured by SP2 averaged 3.2 μg $m^{-3}$, with the peak value of 12.1 μg $m^{-3}$ at 04:26 LT on 7 December. The number of BC-containing particles captured by SPAMS in the size range 200-1200 nm agreed very well with that detected by SP2 ($R^2$ = 0.87). A cluster analysis of the single particle mass spectra allowed for the separation of BC-containing particles into five major classes: (1) Pure BC; (2) BC attributed to biomass burning (BBBC); (3) K-rich BC-containing (KBC); (4) BC internally-mixed with OC and ammonium sulfate (BCOC-SOx); (5) BC internally-mixed with OC and ammonium nitrate (BCOC-NOx). The size distribution of internally-mixed BC particles was bimodal. Detected by SP2, the condensation mode peaked around ~230 nm and droplet mode peaked around ~380 nm, with a clear valley in the size distribution around ~320 nm. The condensation mode mainly consisted of traffic emissions, with particles featuring a small rBC core (~60-80 nm) and a relatively thin absolute coating thickness (ACT, ~50-130 nm). The droplet mode included highly aged traffic emission particles and biomass burning particles. The biomass burning particles

had a larger rBC core (~80-130 nm) and a thick ACT (~110-300 nm). The highly aged traffic emissions had a smaller core (~60-80 nm) and a very thick ACT (~130-300 nm), which is larger than reported in any previous literature. A fast growth rate (~20 nm $h^{-1}$) of rBC with small core sizes was observed during the experiment. High concentrations pollutants like $NO_2$ likely accelerated the aging process and resulted in a continuous size growth of rBC-containing particles from traffic emission.

## 1 Introduction

Aerosols represent the largest uncertainty in estimating radiative forcing of atmospheric species, by strongly affecting the energy balance of the Earth by scattering and/or absorbing solar radiation (Pöschl, 2005), and influencing cloud formation (Jacobson, 2006). Emitted from incomplete combustion of fossil fuel and biomass (Bond et al., 2013), black carbon (BC) is a strongly light-absorbing carbonaceous material in aerosols, second to carbon dioxide as a contributor to positive radiative forcing (Ramanathan and Carmichael, 2008;Jacobson, 2001).

The physical (e.g., size distribution and morphology) and chemical (e.g., mixing state and composition) properties of ambient BC are very complex and are constantly changing in the atmosphere. For example, BC particles exposed to sub-saturated sulfuric acid vapor exhibit a marked change in morphology, characterized by a decreased mobility-based diameter but an increased fractal dimension and effective density (Zhang et al., 2008). By using electron tomography with a transmission electron microscope and three-dimensional (3-D) imaging, Adachi et al. (2010) found that many BC particles have open, chainlike morphology even after being surrounded by organic matter, and are located in off-center positions within their host materials. China et al. (2013) analyzed the morphology of single BC particles using electron microscopy and classified them into four categories: ~50% were embedded (heavily coated), ~34% were partly coated, ~12% had inclusions and ~4% were bare. The organic coating is known to strongly affect the optical properties of the soot aggregates by acting as a lens that amplifies the absorption cross section of the BC core (Lack and Cappa, 2010;Shiraiwa et al., 2010). Schnaiter et al. (2005) observed amplification factors of the internally-mixed BC of 1.8 to 2.1 relative to

the specific absorption cross section of externally-mixed BC. Zhang et al. (2008) observed that the internally-mixed particles can increase their absorption efficiency by nearly 2-fold and scattering efficiency by approximately 10-fold at 80% relative humidity relative to fresh particles. On the other hand, Cappa et al. (2012) and Lan et al. (2013) observed a limited enhancement due to the mixing state of ambient BC, suggesting that other factors may affect their absorption properties. Through coagulation and condensation, BC can form an internal mixture, which increases its cloud nucleation activity (Khalizov et al., 2009;Moffet and Prather, 2009). Most BC is removed from the troposphere via wet deposition with a short lifetime of 5 to 10 days (Kanakidou et al., 2005;Chung and Seinfeld, 2002).

Many measurement methods for refractory BC (rBC) particles have been developed and used in recent years (Petzold et al., 2013). Among them, the Single Particle Soot Photometer (SP2) has become increasingly recognized as a valuable tool for characterizing rBC-containing particles (Stephens et al., 2003;Schwarz et al., 2006). SP2 can quantitatively measure the mass and determine the mixing state of an individual rBC-containing particle (Schwarz et al., 2010). Taylor et al. (2014) evaluated the capability of the SP2 to determine the particle mixing state with help of the concentric core/shell model. Liu et al. (2014) analyzed the size distribution and mixing state of rBC aerosols in London during winter time using the same technique. Furthermore, Moteki et al. (2014) identified two morphological types of the mixed rBC-containing particles as attached and coated, an important finding for understanding the climate impact of rBC particles. Recently, a soot particle aerosol mass spectrometer (SP-AMS) was developed to characterize rBC and non-refractory particulate matter simultaneously (Cross et al., 2010;Onasch et al., 2012;Corbin et al., 2014). SP-AMS was previously used to quantify rBC mass concentration, mixing state and chemical composition in urban environment and biomass burning influenced air (Lee et al., 2015a;Lee et al., 2015b;Willis et al., 2015).

As a highly complementary instrument, single particle aerosol mass spectrometer (SPAMS, not to be confused with the SP-AMS instrument mentioned above) can detect

the chemical properties of BC particles. Moffet and Prather (2009) observed a rapid coating process of organic carbon and sulfate on the BC core and assessed the related absorption enhancement during an air pollution episode of the Mexico City. Healy et al. (2012b) found that the mass size distribution for BC-containing particles was bimodal at an urban background site in Paris. The smaller mode was attributed to local emission, mostly externally-mixed BC particles, while the larger mode was dominated by aged particles associated with continental transport events. Zhang et al. (2014) found that an active photochemical formation of secondary organic aerosol (SOA) led to a distinct diurnal pattern of mixing state of BC with SOA in the condensation mode, while the photochemical aging had limited or negligible influence on the mixing state and growth of BC in the droplet mode. The size ranges of condensation mode (Vacuum Aerodynamic Diameter ($D_{va}$)= ~100-300 nm) and droplet mode ($D_{va}$= ~300- 1000 nm) were defined by John et al. (1990) and Seinfeld and Pandis (2012).

Depending on the experimental method, different terms are used in the literature for the most refractory and light-absorbing components of carbonaceous aerosols: black carbon (BC), refractory black carbon (rBC) and elemental carbon (EC). The definitions of BC, rBC and EC have been discussed in details elsewhere (Bond and Bergstrom, 2006;Almeida et al., 2013;Petzold et al., 2013). In this paper, we use rBC and BC to illustrate the SP2 and SPAMS data, respectively.

All of the studies mentioned above relied on either an SP2 instrument or a single particle aerosol mass spectrometer to characterize BC particles, but not both. Combining these two methods would provide the chemical and physical prosperities of individual BC particles simultaneously and greatly enhance our understanding of their sources and evolution processes. Furthermore, most previous SP2 studies focused on the rBC particles during relatively clean days. Quantitative analysis on the mixing state of BC particles during heavy pollution episodes is still lacking. In this study, we deployed two complementary techniques, with single particle resolution and high time resolution, to detect the evolution of the urban BC aerosols in Shanghai during an extreme pollution period. We used an SP2 instrument to measure the mass and size distribution, and the

mixing state of individual rBC particles. A SPAMS instrument was used in parallel to record chemical characteristics and mixing state of individual BC particles.

# 2 Experimental

## 2.1 Single Particle Soot Photometer

### 2.1.1 Description

The number and mass size distribution, as well as the mixing state of individual rBC particles were characterized using a single particle soot photometer (SP2, Droplet Measurement Technologies, Inc., Boulder, CO) (Stephens et al., 2003;Baumgardner et al., 2004). In brief, SP2 detects incandescence and scattering signals of rBC-containing particles induced by a 1064 nm Nd: YAG intra-cavity laser. The mass of rBC is proportional to the intensity of the laser induced incandescence signal. Any measured particle with a detectable incandescence signal is treated as an rBC particle; whereas a particle that only exhibits scattering signal is considered as a non-rBC particle. The total rBC mass loading is reported as the sum of all detected single rBC masses. The SP2 instrument samples at a low flow rate (30 $cm^3$ $min^{-1}$) in order to avoid multiple particles crossing the laser at the same time. We only saved data for every $50^{th}$ particle in order to extend the sampling time without generating excessively large data sets.

### 2.1.2 Calibration and detection efficiency

The SP2 incandescence signal was calibrated using Aquadag® black carbon particles (Aqueous Deflocculated Acheson Graphite, manufactured by Acheson Inc., USA). The Aquadag® black carbon particles were selected by mobility diameter using a differential mobility analyzer (DMA) and the corresponding particle masses were calculated using the effective density data provided in Gysel et al. (2011) (Fig. S1). The scattering signal was calibrated using mono-disperse polystyrene latex spheres (Nanosphere Size Standards, Duke Scientific Corp., Palo Alto, CA, USA) with known diameters (80–350 nm). More details about the SP2 calibration can be found in Gysel et al. (2011),

Baumgardner et al. (2012) and Laborde et al. (2012). A diagram of the calibration system is shown in the supplement (Fig. S2).

The detection efficiency was measured using Aquadag® black carbon particles, and the results are shown in Fig. S3. The details of the measurement method were described in Schwarz et al. (2010). SP2 detection efficiency was nearly unity for larger rBC particles. The minimum rBC mass that could be observed with near-unity detection efficiency was ~ 0.7 fg rBC, corresponding to 90 nm mass-equivalent diameter; the detection efficiency declined rapidly at lower sizes (Fig. S3). The total ambient mass concentrations of rBC were underestimated because of the low detection efficiency of the smaller rBC particles, likely by ~20 % (Schwarz et al., 2006;McMeeking et al., 2010). During the calibration and sampling time, the SP2 was operated at a stable temperature of 20 ℃ and pressure of ~1013 hPa. The SP2 laser current was around 1750 mA through the whole experiment.

### 2.1.3 Data analysis

The rBC mass in each individual particle was determined from the peak intensity of the incandescence signal according to the Aquadag® black carbon calibration (Sect. 2.1.2). The conversion from the mass to the effective rBC core diameter requires making assumptions about the morphology and effective density of the rBC cores in the particles. Zhang et al. (2015) recently found the ambient rBC cores had an average shape factor of 1.2 and an average density of 1.2 g $cm^{-3}$, suggesting a near- spherical shape with an internal void of 30 % by volume. With the aging process, Zhang et al. (2015) observed that the effective density of BC core increased and the cores transformed to a more compact shape. In this study, we focused on the aged BC-containing particles. Therefore, a density of 1.8 g $cm^{-3}$ was used to convert the ambient rBC mass to the mass equivalent diameter. This value was also recommended in many previous studies (Bond and Bergstrom, 2006;Moteki and Kondo, 2010;Moteki et al., 2010;McMeeking et al., 2011).

In addition to the rBC mass, the measurement of the scattering signal of an rBC-containing particle allows for the determination of its scattering cross section. However, the scattering properties of externally- and internally-mixed rBC particles, as

detected by the SP2, may be distorted, because the mass of each particle is reduced by the laser heating. Thus, scattered light from a sampled rBC particle does not yield a full Gaussian waveform. The Gaussian scattering function was reconstructed from the leading edge of the scattering signal (before the particle is perturbed by the laser), which was measured with a two-element avalanche photodiode (APD). This method allows SP2 to determine the scattering properties of individual rBC particles as well as the rBC mass and to distinguish the mixing state of a single rBC particle (so called, LEO-fit method (Gao et al., 2007)). The optical diameter of a rBC particle or the coated rBC size ($D_p$) was derived by inputting the LEO fitted scattering signal and rBC core size ($D_c$) into Mie calculations with a core refractive index $m$ = 2.26-1.26i (Moteki et al., 2010;Liu et al., 2014;Laborde et al., 2013) and a coating refractive index $m$ = 1.5 + 0i (Laborde et al., 2013). The absolute coating thickness (ACT) of an rBC particle was calculated as ($D_p - D_c$)/2, based on the assumption of a concentric core-shell morphology. However, rBC aging processes in the real atmosphere may result in aerosols with particles that deviate from the core-shell morphology (Matsui et al., 2013). For example, when a small rBC particle coagulates with a relatively large rBC-free particle, the small rBC particle may stay at the surface and lead to an effective negative coating thickness if determined by the methods used here. In this study, the negative coating thickness was observed for less than 2% of all rBC-containing particles; we did not take those particles into account when we calculated the average ACT. More details of data analysis and uncertainties are discussed in supplement, as well as in Liu et al. (2014) and Laborde et al. (2013).

## 2.2 Single Particle Aerosol Mass Spectrometer

A SPAMS instrument (Hexin Analytical Instrument Co., Ltd., Guangdong, China) was deployed simultaneously with SP2 to detect chemical composition of BC-containing particles. The technical details of SPAMS have been described elsewhere (Li et al., 2011). Briefly, aerosols in the size range of 0.2–2.0 μm are introduced into the focus lens through a 0.1 mm critical orifice at a flow of 80 mL $min^{-1}$ due to the pressure drop from ~760 to ~2.2 Torr. Then particles are accelerated to a terminal size-dependent aerodynamic velocity, which is measured by two orthogonally-oriented continuous lasers

(532 nm) separated by a fixed 6.0 cm distance. A pulsed desorption/ionization laser (Q-switched Nd: YAG laser, 266 nm) is triggered when a particle arrives at the ion source region. Both positive and negative ions are detected simultaneously by the time-of-flight mass spectrometer. In this work, the power of the desorption/ionization laser was kept at ~0.6 mJ per pulse. The particle size was calculated from the measured speed using a calibration curve generated for mono-disperse polystyrene latex spheres (Nanosphere Size Standards, Duke Scientific Corp., Palo Alto, CA, USA) with known diameters (0.22–2.00 μm).

All single particle mass spectra were converted into a list of peaks at each *m/z* using TSI MS-Analyze software with a minimum signal threshold of 30 arbitrary units above the baseline. The resulting peak lists were then imported into YAADA (www.yaada.org), a software toolkit in Matlab (version R2012b) for further analysis of particle sizes and chemical components. A total of 385 683 particles were chemically analyzed with both positive and negative ion spectra, accounting for about 56 % of all sized particles. Based on the similarities of the mass-to-charge ratio and peak intensity, particles were clustered by using the ART-2a (adaptive resonance theory) method (Song et al., 1999) with a vigilance factor of 0.85, a learning rate of 0.05 and 20 iterations. Then BC-containing particles, with $D_{va}$ in the size range of 200-1200 nm, were chosen from the clusters, since this size range was consistent with the dominant fraction of BC-containing mass in the atmosphere (Zhang et al., 2014;Healy et al., 2012b). Finally, a total of 86 057 BC-containing particles were grouped into six general particle types according to mass spectral patterns.

## 2.3 Monitor for AeRosols and GAses (MARGA)

A MARGA instrument (ADI 2080, Applikon Analytical B. B. Corp., Netherlands) was used to measure water-soluble inorganic ions in particles. The details of MARGA have been described previously (Jongejan et al., 1995;Du et al., 2011). Briefly, air to be analyzed enters into sample boxes via a $PM_1$ cyclone. The air flow is maintained at 1 $m^3$ $h^{-1}$ by a mass flow controlled air pump. In the sample box, water-soluble gases (HCl, HONO, $SO_2$, $HNO_3$, $NH_3$) are completely absorbed in a dilute solution of hydrogen

peroxide by using a wet rotating denuder (WRD). Aerosols pass through the WRD and are subsequently collected in a steam-jet aerosol collector (SJAC). The two liquid samples with absorbed gases and particles are accumulated in syringes in the analytical box. After filling the syringes for one hour, the samples are then injected into an ion chromatograph (IC). The IC is continuously controlled by an internal calibration method using a standard LiBr solution. In this study, the water-soluble inorganic ions (i.e., $K^+$, $SO_4^{2-}$, $NO_3^-$) in bulk particles were analyzed.

### 2.4 Sampling period and site

The sampling lasted for almost 5 days, from 5 to 10 December, 2013. The instruments were operated in the building of the Department of Environmental Science and Engineering, Fudan University (FDU, 31° 14' N, 121° 29' E) in urban Shanghai, close to both residential and traffic emissions sources. Aerosols were sampled with a $PM_{2.5}$ cyclone positioned 2 m above the roof of the building and transferred to the instruments through a 6 m long stainless steel pipe (45 mm inner diameter). A pump was used to pull air through the sampling system at 30 L $min^{-1}$, minimizing the particle residence time in the sampling line. Aerosols were dried by diffusion drying tubes before they reached the SP2 and SPAMS inlets, which were connected in parallel. The measurement system is presented in Fig. S2. Because of the extremely high particle mass loading, the inlets of SP2 and SPAMS were clogged two times during the sampling period.

## 3 Result and discussion

### 3.1 Overview of the meteorology and air quality

Temporal variations of measured relative humidity, temperature, CO, $O_3$, NO, $NO_2$, $SO_2$, $PM_{2.5}$ and $PM_{10}$ in Shanghai from 12:00 LT on 5 December to 14:00 LT on 10 December are shown in Fig. 1. The meteorology and air quality information were provided by the Shanghai Environmental Monitoring Center, Hongkou Station (http://www.semc.com.cn/aqi/home/Index.aspx). The station is 3.3 km north from the sampling site. The temperature and relative humidity varied between 2-19℃ and 30-100%, with an average of 19℃ and 73%, respectively, during the study. The $O_3$ concentration was relatively low from 18:00 LT on 5 December to 8:00 LT on 7

December. The CO concentration showed two peaks during this period, and its peak value reached 4.1 mg $m^{-3}$ at 14:00 LT on 6 December. The $NO_2$ concentration increased quickly at the beginning, reached 202.5 μg $m^{-3}$ at 21:00 LT on 5 December, and then decreased slowly until 12:00 LT on 7 December. After 12:00 LT on 7 December, the concentrations of $O_3$, CO, $NO_2$ and $SO_2$ fluctuated without an obvious pattern. The concentrations of $O_3$ and $NO_2$ showed the expected anti-correlation, because NO was oxidized to $NO_2$ by $O_3$. The CO concentration was found to correlate reasonably well with rBC mass concentration ($R^2$= 0.59, slope=0.33), as shown in Fig. S4.

The mass loading of $PM_{2.5}$ was extremely high during this period. Its maximum value reached 636 μg $m^{-3}$ at 12:00 LT on 6 December, which was a record-breaking hourly concentration for Shanghai. The daily average concentration was 221 μg $m^{-3}$. Meanwhile, $PM_{10}$ varied from 47 to 691 μg $m^{-3}$, with an average of 252 μg $m^{-3}$. Concentrations of CO, $O_3$, NO, $NO_2$, $SO_2$, $PM_{10}$ and $PM_{2.5}$ during 5-10 December all exceeded the Chinese national ambient air quality standards.

### 3.2 BC size distributions and concentration measurement by SP2

We fitted a log-normal distribution to the rBC core number and mass size measurements during the entire sampling period, as shown in Fig. 2. The number size distribution spanned the range from ~60 to ~400 nm and the peak was around ~60 nm. The measured number concentrations dropped below 60 nm because the SP2 detection efficiency greatly decreases (Sect. 2.1.2) below this particle size. Using the same method, Schwarz et al. (2008) also found that the peak concentration was around 60 nm in boundary layer. The rBC core mass size distribution had a peak around 200 nm, and the majority of the rBC mass was distributed between 70-500 nm.

As shown in Fig. 1, the rBC mass concentration varied from 0.6 μg $m^{-3}$ at 00:02 LT on 10 December to 12.1 μg $m^{-3}$ at 04:26 LT on 7 December, with an average of 3.2 μg $m^{-3}$. The rBC mass concentration observed in Shanghai was similar to other cities in China, e.g., ~4.1 μg $m^{-3}$ in Shenzhen (Huang et al., 2012) and ~3.3 μg $m^{-3}$ in Kaiping (Huang et al., 2011). However, it was much higher than in other mega-cities around the world, e.g.,

~0.9 μg $m^{-3}$ in Paris (Laborde et al., 2013) and ~1.3 μg $m^{-3}$ in London (Liu et al., 2014). All of the values quoted above were based on SP2 measurement so a direct comparison is possible. The rBC mass accounted for 1.45% of $PM_{2.5}$ mass on average in our measurements.

### 3.3 BC particles classification by SPAMS

Classification of particles analyzed by the SPAMS can help elucidate the sources, degree of aging, and mixing state of BC particles. We classified BC-containing particles into six groups according to their mass spectral characteristics. The names of these groups and their number fractions are shown in Table 1. The average mass spectral patterns of each group are shown in Fig. S5.

Pure BC particles only presented strong signals for black carbon fragment ions ($C_n^-$ and $C_n^+$) in both positive and negative ion mass spectra without any signal of secondary species like sulfate or nitrate, suggesting they were fresh BC particles that had not undergone any aging process.

Biomass burning BC-containing (BBBC) particles were characterized by an intense $K^+$ signal for +39 (the charge and *m/z* of the observed ion), +113 ($K_2Cl^+$) and +213 ($K_3SO_4^+$) in the positive ion mass spectra and a strong signal for -26 ($CN^-$) and -42 ($CNO^-$) in the negative ion mass spectra. A significant fragment of levoglucosan, -71 ($C_3H_3O_2^-$), was also observed. Typical black carbon fragments ($C_n^-$) appeared in the negative ion mass spectra. A high signal at -46 ($NO_2^-$), -62 ($NO_3^-$) and a relatively low signal at -97 ($HSO_4^-$) were also observed, suggesting a significant accumulation of nitrate ions on BC particles throughout the air pollution period. The criteria for the identification of BBBC particles is discussed in supplementary section. Potassium-containing soot is a well-established tracer for biomass combustion (Andreae, 1983;Soto-Garcia et al., 2011). Water-soluble $K^+$ in ambient particles measured by an online MARGA method correlated reasonably well with the BBBC particles number ($R^2$=0.64), as shown in Fig. S6. Particles with similar mass spectral patterns were previously observed in several urban field studies and assigned to biomass burning sources (Moffet et al., 2008;Healy et al., 2012b;Bi et al.,

2011).

BC internally-mixed with organic carbon and ammonium sulfate (BCOC-SOx) particles exhibited signals for ammonium +17 ($NH_3^+$), +18 ($NH_4^+$), organic carbon +37 ($C_3H^+$), +43 ($CH_3CO^+$), +50 ($C_4H_2^+$), +51 ($C_4H_3^+$), +61 ($CH_3C(OH)=OH^+$), +62 ($(CH_3)_2NHOH^+$), and a small signal for sodium +23 ($Na^+$) in the positive ion mass spectra, along with black carbon fragment ions ($C_n^+$). There was a high signal for sulfate -97 ($HSO_4^-$) and a relatively low signal for nitrate -46 ($NO_3^-$), -62 ($NO_3^-$) in the negative ion spectra. BC internally-mixed with organic carbon and ammonium nitrate (BCOC-NOx) particles are characterized by very similar positive ion mass spectra to BCOC-SOx, but exhibit lower signals for sulfate and higher signals for nitrate in the negative ion spectra, i.e., -46 ($NO_3^-$), -62 ($NO_3^-$). BC particles with various intensities for organic carbon, nitrate and sulfate were commonly detected in urban ATOFMS field studies (Moffet et al., 2008;Ault et al., 2009;Dall'Osto and Harrison, 2006) and were assigned to traffic emissions (Healy et al., 2012b).

K-rich BC-containing (KBC) particles exhibited strong signals for black carbon fraction in both positive and negative ion mass spectra. This class also had signals for potassium +39 ($K^+$), sodium +23 ($Na^+$) and ammonium +17 ($NH_3^+$), +18 ($NH_4^+$) in positive ion mass spectra and nitrate -46 ($NO_2^-$), -62 ($NO_3^-$), and sulfate -97 ($HSO_4^-$) in the negative ion mass spectra. This class was detected from diesel vehicle emissions in a previous study by (Li et al., 2013). The KBC exhibited pronounced diurnal variation, with two major peaks during early morning (4:00- 7:00 LT) and night hours (20:00- 22:00 LT) (Fig. S7). Shanghai municipal government regulates that the heavily loaded diesel trucks cannot go into downtown area from 7:00- 20:00 LT. The diurnal variation of KBC is consistent with the traffic flow of diesel trucks based on our results.

NOx can be used as a tracer of local traffic emissions in urban areas. In this study, the NOx concentrations agreed well with the sum of KBC, BCOC-NOx and BCOC-SOx particles numbers ($R^2$=0.65) (Fig. S8). Based on the above analysis, we believed that the BBBC came from biomass burning, KBC, and BCOC-NOx and BCOC-SOx came from traffic emissions.

We should note that SPAMS preferentially detected internally-mixed BC particles, and had reduced detection efficiency for pure BC particles. The particles detected and chemically analyzed by SPAMS range from 200 to 2000 nm in size, and the detection efficiency decreases rapidly below 400 nm and above 1200 nm (Li et al., 2011). The majority of the pure BC particles diameter are smaller than 200 nm in diameter (Kondo et al., 2006), and therefore, they are missed by SPAMS.

## 3.4 Mixing state and size distribution of internally-mixed BC particles

### 3.4.1 Temporal variations of internally-mixed BC particles

A comparison of the internally-mixed BC particles number concentration between SP2 and SPAMS is given in Fig. 3. The agreement observed is reasonably good ($R^2 = 0.87$) considering the combined experimental uncertainties of the methods and the different cut-off diameters of SP2 ($D_p$ >170 nm) and SPAMS (200 nm <$D_{va}$ <1200 nm). Detected by SP2, the internally-mixed rBC particles accounted for approximately 70% number fraction of BC-containing particles during the whole period. Moteki et al. (2007) also found the internally-mixed rBC particles accounted for 63% number fraction of BC-containing particles in the aged urban plume. The high correlation coefficient indicates that we can use the two complementary techniques to analyze the mixing state and chemical composition of internally-mixed BC particles with single particle resolution at the same time (although not for the same particle since both methods are destructive).

The temporal variation of number size distribution and particle types changed rapidly and intricately, as shown in Fig. 4. From 12:00 LT on 5 December to 00:00 LT on 7 December, the $PM_{2.5}$ and rBC mass increased slowly to an extremely polluted state. The number fraction of BBBC particles also increased during this period (Fig. 4(b)) and $D_p$ of rBC showed two distinct modes (Fig. 4(a)). Then, the BC-containing particles number increased rapidly at 02:00 LT on 7 December. Presumably, boundary layer compression during the night led the fast change of BC-containing particles. After that, the number concentration of BC-containing particles exhibited diurnal variation, with two major peaks at the rush hours, i.e., from 8:00-12:00 LT or from 16:00-20:00 LT.

### 3.4.2 Size distribution and source apportionments of internally-mixed BC particles

Fig. 5(a) shows the entire diameter ($D_p$) number size distribution histogram of internally-mixed rBC particles detected by SP2 during the entire sampling period. The BC-containing particles were detected in both the condensation and droplet modes in this study. Since the two modes are overlapped, it is possible that some of the particles in the droplet mode are from the tail of condensation mode. Here, we used the minimum value between the two peaks in Fig. 5(a) (black line) and its corresponding $D_p$ (320 nm) as the separation of the condensation mode and droplet mode. We added this separation line in Fig. 5(c) to separate the condensation mode particles (left side) and the droplet mode particles (right side). The condensation mode peak was centered around ~230 nm and droplet mode peak was centered around ~380 nm. The presence of condensation mode ($D_{va}$= ~200-500 nm) and droplet mode ($D_{va}$= ~550-1200 nm) was confirmed by the SPAMS data (Fig. 5(b)). Here the SPAMS size distribution was based on the number fraction of BC-containing particles in all detected particles. Similar particle size distributions were also found in other studies in China (Huang and Yu, 2008;Zhang et al., 2014).

The specific composition in condensation and droplet modes were quite different (Fig.5 (b)). BBBC particles exhibited a higher number fraction in the droplet mode than in the condensation mode. Ammonium nitrate can condense on particle surfaces during atmospheric transport if sulfate is fully neutralized and excess ammonia is available (Riemer et al., 2004). The sulfate condensation on BC surfaces occurs soon after the BC emission, while ammonium nitrate condensation occurs over longer timescales during transport (Healy et al., 2012a). In this work, most KBC and BBBC particles and all the BCOC-NOx particles showed stronger $NO_3^-$ signals than $SO_4^-$ signals (as shown in Fig. S5), suggesting that most BC-containing were deeply aged. Based on the particle classification and source apportionment analysis, the internally-mixed BC particles from traffic emissions accounted for almost all of the particles observed in the condensation

399 mode. However, the particle sources in the droplet mode were more diverse, including
400 traffic emissions and biomass burning.

401 Previous studies revealed that different sources emit different core diameters for
402 rBC-containing particles (Liu et al., 2014;Takahama et al., 2014;Reddington et al.,
403 2013;Schwarz et al., 2008) and the aging processes affect the coating thickness (Laborde
404 et al., 2013;Liu et al., 2014). We identified the sources and estimated aging process of
405 rBC-containing particles by using 2-D image plot "fingerprint" of $D_c$ and absolute
406 coating thickness (ACT) information. Fig. 5(c) shows the dependence of ACT on $D_c$,
407 weighed by the number concentration. In the condensation mode, the particles were
408 characterized by small $D_c$ values (~60-80 nm) with thin ACT (~50-130 nm). In
409 combination with the SPAMS information, these particles with small $D_c$ and thin ACT
410 should be mainly from the traffic sources (Fig. 5(b)).

411 However, the droplet mode was very different from the condensation mode and showed a
412 diversity of sources. In the droplet mode, the "fingerprint" showed two peaks in the size
413 distribution. The first peak had small $D_c$ values (~60-80 nm) and thick ACT (~130-300
414 nm). We assume that the rBC-containing particles in the first peak were from traffic
415 emissions. In previous studies, the particles associated with traffic emissions had small
416 core sizes and thin coating thickness (Laborde et al., 2013;Liu et al., 2014). However, in
417 this study, we found that the rBC-containing particles from traffic could be highly-aged,
418 resulting in a much thicker coating than previously observed. This could be because
419 polluted air masses promote faster rBC aging processes (Matsui et al., 2013). The second
420 peak showed larger $D_c$ (~80-130 nm) and thick ACT (~110-300 nm). These particles
421 were presumably from biomass burning. It has been reported using SP2 measurements
422 that fresh biomass burning rBC particles are thickly coated (Schwarz et al., 2008;Sahu et
423 al., 2012;Liu et al., 2014).

424 Since there was no clear-cut separation between traffic emissions and biomass burning
425 rBC-containing particles in the droplet mode, it was hard to distinguish them when we
426 just used the core and shell information from SP2 (Liu et al., 2014). We selected
427 SP2-detected particles with larger core sizes (80-130 nm) and thicker coating (120-300

nm) and compared with the biomass burning particles number concentration from SPAMS, as shown in Fig. S9. The good correlation ($R^2$ = 0.71) verified the conclusion that the rBC-containing particles with larger cores and thicker coating were from biomass burning. Even though these larger rBC-containing particles only accounted for less than 20% number fraction, they are likely to be more hygroscopic (Liu et al., 2013;Wang et al., 2014) and be scavenged by wet deposition (Moteki et al., 2012). Such particles will have greater potential to enhance the semi-direct effect (Koch and Del Genio, 2010) through interaction with cloud processes.

The diversity of sources of the droplet mode BC-containing particles was also detected in SPAMS, as we discussed before. SPAMS data showed that the internally-mixed BC particles from traffic emissions were more abundant in the droplet mode than those form biomass burning (Fig. 5(b)). However, the SP2 data showed that particles with a small core and thick ACT (major traffic emission) were less abundant than particles with a larger core with thick ACT (major biomass burning) (Fig. 5(c)). As we discussed in part 2.1.2, rBC-containing particle with smaller cores are not efficiently detected by SP2, which may result in an underestimation of the fraction of traffic emission of rBC-containing particles in the droplet mode.

The aging of traffic-emitted rBC-containing particles during the heavy air pollution episode (12:00 LT, 5 December 2013 – 12:00 LT, 7 December 2013) was elucidated using the temporal variation of relative coating thickness (RCT, entire particle diameter/rBC core diameter, $D_p/D_c$) of rBC-containing particles ($D_c$ = 60-80 nm), as shown in Fig. 6a. Note that we could only obtain optical sizing information from sufficiently coated particles because of the SP2 minimal detectable optical diameter of ~170 nm. From 16:00 LT to 22:00 LT on 5 December, the RCT of rBC-containing particles and $PM_{2.5}$ concentration grew rapidly. Even though the SP2's inlet was blocked from 23:00 LT on 5 December to 10:00 LT on 6 December due to the extremely high PM mass loading, the data collected around that time suggest the rBC-containing particles growth was continuous until 13:00 LT on 6 December. The absolute coating growth rate

456 was around 20 nm/hour during this period (16:00 LT, 5 December – 13:00 LT, 6
457 December).

458 Variations of the major chemical species in the vehicle-emitted BC-containing particles
459 (selected by SPAMS) were also analyzed. The relative peak areas of nitrate -63 ($NO_3^-$)
460 and organic carbon (i.e., +27 ($C_2H_3^+$), +43 ($CH_3CO^+$)) showed a relatively high level
461 during 16:00 LT on 5 December- 13:00 LT on 6 December (Fig. 6(b)). Guo et al. (2014)
462 observed that gaseous emissions of volatile organic compounds, nitrogen oxides from
463 urban transportation and sulfur dioxide from region industry were responsible for large
464 secondary particle matter formation in Beijing. Fig. S10 shows the mass concentrations
465 of $SO_2$, $NO_2$, the mass ratio of $NO_2/SO_2$, MARGA-measured mass concentrations of
466 particulate sulfate and nitrate, and the mass ratio of $NO_3^-/SO_4^{2-}$ in $PM_1$ during the whole
467 sampling period. The average mass ratios of $NO_2/SO_2$ in gas phase and $NO_3^-/SO_4^{2-}$ in
468 particles phase were 2.8 and 1.4 respectively. During the heavy air pollution episode
469 (12:00 LT, 5 December 2013 – 13:00 LT, 6 December 2013), both $NO_2$ and particulate
470 nitrate increased dramatically along with the traffic emitted BC particle growth (as shown
471 Fig. 6), while the $SO_2$ and particulate sulfate had a slight increase and remained at a
472 relatively lower level. Apparently, the gas to particle conversion of $NO_2$ to nitrate played
473 a more important role than the condensation of $SO_2$ in the particle growth during this
474 pollution episode. In the previous field studies (Huebert et al., 1988;Yao et al., 2002), the
475 high mass ratio of $NO_3^-/SO_4^{2-}$ (>1.0) was regarded as a sign of dominant traffic emission.
476 Wang et al. (2015) found that the high mass ratio of $NO_2/SO_2$ resulting from traffic
477 emissions was a major reason in triggering the heavy haze in Shanghai. In this work, the
478 evaluation of BC-containing particles also suggested that high concentrations of $NO_2$ and
479 possibly volatile organics and their transformations play a vital role for particle growth
480 and the increase of PM loading in urban area especially during a heavy pollution episode.
481 Reductions in the emissions of gaseous precursors are critical for remediation of the
482 severe urban haze pollution in China.

483 **4 Conclusions**

In this study, we characterized BC-containing particles during a heavy air pollution episode in Shanghai. The rBC mass loading in Shanghai was similar to other cities in China but much higher than in other mega-cities around the world, with an average of 3.2 μg $m^{-3}$ and the peak value of 12.1 μg $m^{-3}$ at 04:26 LT on 7 December 2013. The rBC mass accounted for 1.45% of $PM_{2.5}$ mass on average. The number- and mass-weighted BC core size distributions were around ~60-400 and 70-500 nm, with peaks around ~60 and ~200 nm, respectively.

Using SPAMS, we classified the BC-containing particles into 6 groups, according to their mass spectral patterns. The pure BC particles accounted for 0.62% number fraction of BC-containing particles (although this number could be underestimated because of the low detection efficiency for pure BC in SPAMS). The BBBC particles from biomass burning accounted for 25.57%. The KBC, BCOC-NOx and BCOC-SOx from traffic emissions accounted for 70.18%. The remaining unidentified particles accounted for 3.63%.

The size distribution of internally-mixed rBC particles was bimodal. The condensation mode mainly consisted of traffic emissions, which had a small core (~60-80 nm) with thin ACT (~50-130 nm). The droplet mode included biomass burning and deeply aged traffic-emitted rBC-containing particles. The biomass burning particles had larger core sizes (~80-130 nm) with thick ACT (~110-300 nm) and the highly aged traffic emissions had small core sizes (~60-80 nm) with thick ACT (~130-300 nm). It is rare to see the traffic-emitted rBC growing so quickly to the droplet mode. The high concentration of $NO_2$ and its rapid conversion to particulate nitrate accelerated the growth of BC-containing particles and contributed to the high particle mass concentration during this heavy air pollution episode.

The quantitative number and mass information provided by SP2 supplemented the SPAMS chemical analysis in the entire experiment. The two complementary techniques can detect the physical and chemical properties of BC aerosol with single particle resolution. The combined use of SP2 and SPAMS have great promise for wider applications in future atmospheric measurements.

## Acknowledgments

This work was supported by the National Natural Science Foundation of China (91544224, 41275126), the Ministry of Science & Technology of China (2012YQ220113-4), the Science & Technology Commission of Shanghai Municipality (14XD1400600), the Ministry of Environmental Protection of China (201409008).

## References


Adachi, K., Chung, S. H., and Buseck, P. R.: Shapes of soot aerosol particles and implications for their effects on climate, Journal of Geophysical Research: Atmospheres, 115, D15206, 10.1029/2009JD012868, 2010.

Almeida, J., Schobesberger, S., Kurten, A., Ortega, I. K., Kupiainen-Maatta, O., Praplan, A. P., Adamov, A., Amorim, A., Bianchi, F., Breitenlechner, M., David, A., Dommen, J., Donahue, N. M., Downard, A., Dunne, E., Duplissy, J., Ehrhart, S., Flagan, R. C., Franchin, A., Guida, R., Hakala, J., Hansel, A., Heinritzi, M., Henschel, H., Jokinen, T., Junninen, H., Kajos, M., Kangasluoma, J., Keskinen, H., Kupc, A., Kurten, T., Kvashin, A. N., Laaksonen, A., Lehtipalo, K., Leiminger, M., Leppa, J., Loukonen, V., Makhmutov, V., Mathot, S., McGrath, M. J., Nieminen, T., Olenius, T., Onnela, A., Petaja, T., Riccobono, F., Riipinen, I., Rissanen, M., Rondo, L., Ruuskanen, T., Santos, F. D., Sarnela, N., Schallhart, S., Schnitzhofer, R., Seinfeld, J. H., Simon, M., Sipila, M., Stozhkov, Y., Stratmann, F., Tome, A., Trostl, J., Tsagkogeorgas, G., Vaattovaara, P., Viisanen, Y., Virtanen, A., Vrtala, A., Wagner, P. E., Weingartner, E., Wex, H., Williamson, C., Wimmer, D., Ye, P. L., Yli-Juuti, T., Carslaw, K. S., Kulmala, M., Curtius, J., Baltensperger, U., Worsnop, D. R., Vehkamaki, H., and Kirkby, J.: Molecular understanding of sulphuric acid-amine particle nucleation in the atmosphere, Nature, 502, 359-+, 10.1038/nature12663, 2013.

Andreae, M. O.: Soot Carbon and Excess Fine Potassium: Long-Range Transport of Combustion-Derived Aerosols, Science, 220, 1148-1151, 10.1126/science.220.4602.1148, 1983.

Ault, A. P., Moore, M. J., Furutani, H., and Prather, K. A.: Impact of Emissions from the Los Angeles Port Region on San Diego Air Quality during Regional Transport Events, Environmental Science & Technology, 43, 3500-3506, 10.1021/es8018918, 2009.

Baumgardner, D., Kok, G., and Raga, G.: Warming of the Arctic lower stratosphere by light absorbing particles, Geophysical Research Letters, 31, 10.1029/2003gl018883, 2004.

Baumgardner, D., Popovicheva, O., Allan, J., Bernardoni, V., Cao, J., Cavalli, F., Cozic, J., Diapouli, E., Eleftheriadis, K., Genberg, P. J., Gonzalez, C., Gysel, M., John, A., Kirchstetter, T. W., Kuhlbusch, T. A. J., Laborde, M., Lack, D., Muller, T., Niessner, R., Petzold, A., Piazzalunga, A., Putaud, J. P., Schwarz, J., Sheridan, P., Subramanian, R., Swietlicki, E., Valli, G., Vecchi, R., and

550 Viana, M.: Soot reference materials for instrument calibration and intercomparisons: a
551 workshop summary with recommendations, Atmos. Meas. Tech., 5, 1869-1887,
552 10.5194/amt-5-1869-2012, 2012.
553 Bi, X. H., Zhang, G. H., Li, L., Wang, X. M., Li, M., Sheng, G. Y., Fu, J. M., and Zhou, Z.: Mixing
554 state of biomass burning particles by single particle aerosol mass spectrometer in the
555 urban area of PRD, China, Atmos. Environ., 45, 3447-3453,
556 10.1016/j.atmosenv.2011.03.034, 2011.
557 Bond, T. C., and Bergstrom, R. W.: Light absorption by carbonaceous particles: An
558 investigative review, Aerosol Sci. Technol., 40, 27-67, 10.1080/02786820500421521, 2006.
559 Bond, T. C., Doherty, S. J., Fahey, D. W., Forster, P. M., Berntsen, T., DeAngelo, B. J., Flanner, M.
560 G., Ghan, S., Karcher, B., Koch, D., Kinne, S., Kondo, Y., Quinn, P. K., Sarofim, M. C., Schultz, M.
561 G., Schulz, M., Venkataraman, C., Zhang, H., Zhang, S., Bellouin, N., Guttikunda, S. K., Hopke, P.
562 K., Jacobson, M. Z., Kaiser, J. W., Klimont, Z., Lohmann, U., Schwarz, J. P., Shindell, D.,
563 Storelvmo, T., Warren, S. G., and Zender, C. S.: Bounding the role of black carbon in the
564 climate system: A scientific assessment, Journal of Geophysical Research-Atmospheres, 118,
565 5380-5552, 10.1002/jgrd.50171, 2013.
566 Cappa, C. D., Onasch, T. B., Massoli, P., Worsnop, D. R., Bates, T. S., Cross, E. S., Davidovits, P.,
567 Hakala, J., Hayden, K. L., Jobson, B. T., Kolesar, K. R., Lack, D. A., Lerner, B. M., Li, S. M., Mellon,
568 D., Nuaaman, I., Olfert, J. S., Petaja, T., Quinn, P. K., Song, C., Subramanian, R., Williams, E. J.,
569 and Zaveri, R. A.: Radiative Absorption Enhancements Due to the Mixing State of
570 Atmospheric Black Carbon, Science, 337, 1078-1081, 10.1126/science.1223447, 2012.
571 China, S., Mazzoleni, C., Gorkowski, K., Aiken, A. C., and Dubey, M. K.: Morphology and mixing
572 state of individual freshly emitted wildfire carbonaceous particles, Nature communications,
573 4, 2013.
574 Chung, S. H., and Seinfeld, J. H.: Global distribution and climate forcing of carbonaceous
575 aerosols, Journal of Geophysical Research: Atmospheres, 107, 4407,
576 10.1029/2001JD001397, 2002.
577 Corbin, J. C., Sierau, B., Gysel, M., Laborde, M., Keller, A., Kim, J., Petzold, A., Onasch, T. B.,
578 Lohmann, U., and Mensah, A. A.: Mass spectrometry of refractory black carbon particles
579 from six sources: carbon-cluster and oxygenated ions, Atmos. Chem. Phys., 14, 2591-2603,

580 10.5194/acp-14-2591-2014, 2014.
581 Cross, E. S., Onasch, T. B., Ahern, A., Wrobel, W., Slowik, J. G., Olfert, J., Lack, D. A., Massoli, P.,
582 Cappa, C. D., Schwarz, J. P., Spackman, J. R., Fahey, D. W., Sedlacek, A., Trimborn, A., Jayne, J. T.,
583 Freedman, A., Williams, L. R., Ng, N. L., Mazzoleni, C., Dubey, M., Brem, B., Kok, G.,
584 Subramanian, R., Freitag, S., Clarke, A., Thornhill, D., Marr, L. C., Kolb, C. E., Worsnop, D. R.,
585 and Davidovits, P.: Soot Particle Studies Instrument Inter-ComparisonProject Overview,
586 Aerosol Sci. Technol., 44, 592-611, 10.1080/02786826.2010.482113, 2010.
587 Dall'Osto, M., and Harrison, R. M.: Chemical characterisation of single airborne particles in
588 Athens (Greece) by ATOFMS, Atmos. Environ., 40, 7614-7631,
589 http://dx.doi.org/10.1016/j.atmosenv.2006.06.053, 2006.
590 Du, H., Kong, L., Cheng, T., Chen, J., Du, J., Li, L., Xia, X., Leng, C., and Huang, G.: Insights into
591 summertime haze pollution events over Shanghai based on online water-soluble ionic
592 composition of aerosols, Atmos. Environ., 45, 5131-5137,
593 http://dx.doi.org/10.1016/j.atmosenv.2011.06.027, 2011.
594 Gao, R., Schwarz, J., Kelly, K., Fahey, D., Watts, L., Thompson, T., Spackman, J., Slowik, J., Cross,
595 E., and Han, J.-H.: A novel method for estimating light-scattering properties of soot aerosols
596 using a modified single-particle soot photometer, Aerosol Sci. Technol., 41, 125-135, 2007.
597 Guo, S., Hu, M., Zamora, M. L., Peng, J., Shang, D., Zheng, J., Du, Z., Wu, Z., Shao, M., Zeng, L.,
598 Molina, M. J., and Zhang, R.: Elucidating severe urban haze formation in China, Proc. Nat.
599 Acad. Sci., 111, 17373-17378, 2014.
600 Gysel, M., Laborde, M., Olfert, J. S., Subramanian, R., and Grohn, A. J.: Effective density of
601 Aquadag and fullerene soot black carbon reference materials used for SP2 calibration,
602 Atmos. Meas. Tech., 4, 2851-2858, 10.5194/amt-4-2851-2011, 2011.
603 Healy, R. M., Chen, Y., Kourtchev, I., Kalberer, M., O'Shea, D., and Wenger, J. C.: Rapid
604 Formation of Secondary Organic Aerosol from the Photolysis of 1-Nitronaphthalene: Role of
605 Naphthoxy Radical Self-reaction, Environmental Science & Technology, 46, 11813-11820,
606 10.1021/es302841j, 2012a.
607 Healy, R. M., Sciare, J., Poulain, L., Kamili, K., Merkel, M., Muller, T., Wiedensohler, A.,
608 Eckhardt, S., Stohl, A., Sarda-Esteve, R., McGillicuddy, E., O'Connor, I. P., Sodeau, J. R., and
609 Wenger, J. C.: Sources and mixing state of size-resolved elemental carbon particles in a

European megacity: Paris, Atmospheric Chemistry and Physics, 12, 1681-1700, 10.5194/acp-12-1681-2012, 2012b.

Huang, X. F., and Yu, J. Z.: Size distributions of elemental carbon in the atmosphere of a coastal urban area in South China: characteristics, evolution processes, and implications for the mixing state, Atmospheric Chemistry and Physics, 8, 5843-5853, 2008.

Huang, X. F., Gao, R. S., Schwarz, J. P., He, L. Y., Fahey, D. W., Watts, L. A., McComiskey, A., Cooper, O. R., Sun, T. L., Zeng, L. W., Hu, M., and Zhang, Y. H.: Black carbon measurements in the Pearl River Delta region of China, Journal of Geophysical Research-Atmospheres, 116, 10.1029/2010jd014933, 2011.

Huang, X. F., Sun, T. L., Zeng, L. W., Yu, G. H., and Luan, S. J.: Black carbon aerosol characterization in a coastal city in South China using a single particle soot photometer, Atmos. Environ., 51, 21-28, 10.1016/j.atmosenv.2012.01.056, 2012.

Huebert, B., Mingxing, W., and Weixiu, L.: Atmospheric nitrate, sulfate, ammonium and calcium concentrations in China, Tellus B, 40, 1988.

Jacobson, M. Z.: Strong radiative heating due to the mixing state of black carbon in atmospheric aerosols, Nature, 409, 695-697, http://www.nature.com/nature/journal/v409/n6821/suppinfo/409695a0_S1.html, 2001.

Jacobson, M. Z.: Effects of Externally-Through-Internally-Mixed Soot Inclusions within Clouds and Precipitation on Global Climate†, The Journal of Physical Chemistry A, 110, 6860-6873, 10.1021/jp056391r, 2006.

John, W., Wall, S. M., Ondo, J. L., and Winklmayr, W.: MODES IN THE SIZE DISTRIBUTIONS OF ATMOSPHERIC INORGANIC AEROSOL, Atmospheric Environment Part a-General Topics, 24, 2349-2359, 10.1016/0960-1686(90)90327-j, 1990.

Jongejan, P., Bai, Y., Veltkamp, A., Wye, G., and Slaninaa, J.: An Automated Field Instrument for The Determination of Acidic Gases in Air, Int. J. Environ. Anal. Chem., 66, 241-251, 1995.

Kanakidou, M., Seinfeld, J. H., Pandis, S. N., Barnes, I., Dentener, F. J., Facchini, M. C., Van Dingenen, R., Ervens, B., Nenes, A., Nielsen, C. J., Swietlicki, E., Putaud, J. P., Balkanski, Y., Fuzzi, S., Horth, J., Moortgat, G. K., Winterhalter, R., Myhre, C. E. L., Tsigaridis, K., Vignati, E., Stephanou, E. G., and Wilson, J.: Organic aerosol and global climate modelling: a review, Atmos. Chem. Phys., 5, 1053-1123, 10.5194/acp-5-1053-2005, 2005.

Khalizov, A. F., Zhang, R., Zhang, D., Xue, H., Pagels, J., and McMurry, P. H.: Formation of highly hygroscopic soot aerosols upon internal mixing with sulfuric acid vapor, Journal of Geophysical Research: Atmospheres, 114, D05208, 10.1029/2008JD010595, 2009.

Koch, D., and Del Genio, A. D.: Black carbon semi-direct effects on cloud cover: review and synthesis, Atmospheric Chemistry and Physics, 10, 7685-7696, 10.5194/acp-10-7685-2010, 2010.

Kondo, Y., Komazaki, Y., Miyazaki, Y., Moteki, N., Takegawa, N., Kodama, D., Deguchi, S., Nogami, M., Fukuda, M., Miyakawa, T., Morino, Y., Koike, M., Sakurai, H., and Ehara, K.: Temporal variations of elemental carbon in Tokyo, Journal of Geophysical Research: Atmospheres, 111, D12205, 10.1029/2005JD006257, 2006.

Laborde, M., Schnaiter, M., Linke, C., Saathoff, H., Naumann, K. H., Mohler, O., Berlenz, S., Wagner, U., Taylor, J. W., Liu, D., Flynn, M., Allan, J. D., Coe, H., Heimerl, K., Dahlkotter, F., Weinzierl, B., Wollny, A. G., Zanatta, M., Cozic, J., Laj, P., Hitzenberger, R., Schwarz, J. P., and Gysel, M.: Single Particle Soot Photometer intercomparison at the AIDA chamber, Atmos. Meas. Tech., 5, 3077-3097, 10.5194/amt-5-3077-2012, 2012.

Laborde, M., Crippa, M., Tritscher, T., Jurányi, Z., Decarlo, P. F., Temime-Roussel, B., Marchand, N., Eckhardt, S., Stohl, A., Baltensperger, U., Prévôt, A. S. H., Weingartner, E., and Gysel, M.: Black carbon physical properties and mixing state in the European megacity Paris, Atmos. Chem. Phys., 13, 5831-5856, 10.5194/acp-13-5831-2013, 2013.

Lack, D. A., and Cappa, C. D.: Impact of brown and clear carbon on light absorption enhancement, single scatter albedo and absorption wavelength dependence of black carbon, Atm. Chem. Phys., 10, 4207-4220, 10.5194/acp-10-4207-2010, 2010.

Lan, Z. J., Huang, X. F., Yu, K. Y., Sun, T. L., Zeng, L. W., and Hu, M.: Light absorption of black carbon aerosol and its enhancement by mixing state in an urban atmosphere in South China, Atmos. Environ., 69, 118-123, 10.1016/j.atmosenv.2012.12.009, 2013.

Lee, A. K. Y., Willis, M. D., Healy, R. M., Onasch, T. B., and Abbatt, J. P. D.: Mixing state of carbonaceous aerosol in an urban environment: single particle characterization using the soot particle aerosol mass spectrometer (SP-AMS), Atmos. Chem. Phys., 15, 1823-1841, 10.5194/acp-15-1823-2015, 2015a.

Lee, A. K. Y., Willis, M. D., Healy, R. M., Wang, J. M., Jeong, C. H., Wenger, J. C., Evans, G. J., and

Abbatt, J. P. D.: Single particle characterization of biomass burning organic aerosol (BBOA): evidence for non-uniform mixing of high molecular weight organics and potassium, Atmos. Chem. Phys. Discuss., 15, 32157-32183, 10.5194/acpd-15-32157-2015, 2015b.

Li, L., Huang, Z., Dong, J., Li, M., Gao, W., Nian, H., Fu, Z., Zhang, G., Bi, X., Cheng, P., and Zhou, Z.: Real time bipolar time-of-flight mass spectrometer for analyzing single aerosol particles, International Journal of Mass Spectrometry, 303, 118-124, http://dx.doi.org/10.1016/j.ijms.2011.01.017, 2011.

Li, L., Tan, G. B., Zhang, L., Fu, Z., Nian, H. Q., Huang, Z. X., Zhou, Z., and Li, M.: Analysis of Diesel Exhaust Particles Using Single Particle Aerosol Mass Spectrometry, Chinese Journal of Analytical Chemistry, 41, 1831-1836, 10.3724/sp.j.1096.2013.30545, 2013.

Liu, D., Allan, J., Whitehead, J., Young, D., Flynn, M., Coe, H., McFiggans, G., Fleming, Z. L., and Bandy, B.: Ambient black carbon particle hygroscopic properties controlled by mixing state and composition, Atmospheric Chemistry and Physics, 13, 2015-2029, 10.5194/acp-13-2015-2013, 2013.

Liu, D., Allan, J. D., Young, D. E., Coe, H., Beddows, D., Fleming, Z. L., Flynn, M. J., Gallagher, M. W., Harrison, R. M., Lee, J., Prevot, A. S. H., Taylor, J. W., Yin, J., Williams, P. I., and Zotter, P.: Size distribution, mixing state and source apportionments of black carbon aerosols in London during winter time, Atmos. Chem. Phys. Discuss., 14, 16291-16349, 10.5194/acpd-14-16291-2014, 2014.

Matsui, H., Koike, M., Kondo, Y., Moteki, N., Fast, J. D., and Zaveri, R. A.: Development and validation of a black carbon mixing state resolved three-dimensional model: Aging processes and radiative impact, Journal of Geophysical Research: Atmospheres, 118, 2304-2326, 10.1029/2012JD018446, 2013.

McMeeking, G. R., Hamburger, T., Liu, D., Flynn, M., Morgan, W. T., Northway, M., Highwood, E. J., Krejci, R., Allan, J. D., Minikin, A., and Coe, H.: Black carbon measurements in the boundary layer over western and northern Europe, Atmospheric Chemistry and Physics, 10, 9393-9414, 10.5194/acp-10-9393-2010, 2010.

McMeeking, G. R., Morgan, W. T., Flynn, M., Highwood, E. J., Turnbull, K., Haywood, J., and Coe, H.: Black carbon aerosol mixing state, organic aerosols and aerosol optical properties over the United Kingdom, Atmospheric Chemistry and Physics, 11, 9037-9052,

10.5194/acp-11-9037-2011, 2011.
Moffet, R. C., de Foy, B., Molina, L. T., Molina, M. J., and Prather, K. A.: Measurement of ambient aerosols in northern Mexico City by single particle mass spectrometry, Atmospheric Chemistry and Physics, 8, 4499-4516, 2008.
Moffet, R. C., and Prather, K. A.: In-situ measurements of the mixing state and optical properties of soot with implications for radiative forcing estimates, Proceedings of the National Academy of Sciences of the United States of America, 106, 11872-11877, 10.1073/pnas.0900040106, 2009.
Moteki, N., Kondo, Y., Miyazaki, Y., Takegawa, N., Komazaki, Y., Kurata, G., Shirai, T., Blake, D., Miyakawa, T., and Koike, M.: Evolution of mixing state of black carbon particles: Aircraft measurements over the western Pacific in March 2004, Geophysical research letters, 34, 2007.
Moteki, N., and Kondo, Y.: Dependence of laser-induced incandescence on physical properties of black carbon aerosols: Measurements and theoretical interpretation, Aerosol Sci. Technol., 44, 663-675, 2010.
Moteki, N., Kondo, Y., and Nakamura, S.: Method to measure refractive indices of small nonspherical particles: Application to black carbon particles, Journal of Aerosol Science, 41, 513-521, 10.1016/j.jaerosci.2010.02.013, 2010.
Moteki, N., Kondo, Y., Oshima, N., Takegawa, N., Koike, M., Kita, K., Matsui, H., and Kajino, M.: Size dependence of wet removal of black carbon aerosols during transport from the boundary layer to the free troposphere, Geophysical Research Letters, 39, L13802, 10.1029/2012GL052034, 2012.
Moteki, N., Kondo, Y., and Adachi, K.: Identification by single - particle soot photometer of black carbon particles attached to other particles: Laboratory experiments and ground observations in Tokyo, Journal of Geophysical Research: Atmospheres, 2014.
Onasch, T. B., Trimborn, A., Fortner, E. C., Jayne, J. T., Kok, G. L., Williams, L. R., Davidovits, P., and Worsnop, D. R.: Soot Particle Aerosol Mass Spectrometer: Development, Validation, and Initial Application, Aerosol Sci. Technol., 46, 804-817, 10.1080/02786826.2012.663948, 2012.
Petzold, A., Ogren, J., Fiebig, M., Laj, P., Li, S.-M., Baltensperger, U., Holzer-Popp, T., Kinne, S.,

730 Pappalardo, G., and Sugimoto, N.: Recommendations for reporting" black carbon"
731 measurements, Atmospheric Chemistry and Physics, 13, 8365-8379, 2013.
732 Pöschl, U.: Atmospheric aerosols: Composition, transformation, climate and health effects,
733 Angewandte Chemie International Edition, 44, 7520-7540, 2005.
734 Ramanathan, V., and Carmichael, G.: Global and regional climate changes due to black
735 carbon, Nature geoscience, 1, 221-227, 2008.
736 Reddington, C. L., McMeeking, G., Mann, G. W., Coe, H., Frontoso, M. G., Liu, D., Flynn, M.,
737 Spracklen, D. V., and Carslaw, K. S.: The mass and number size distributions of black carbon
738 aerosol over Europe, Atmospheric Chemistry and Physics, 13, 4917-4939,
739 10.5194/acp-13-4917-2013, 2013.
740 Riemer, N., Vogel, H., and Vogel, B.: Soot aging time scales in polluted regions during day and
741 night, Atmos. Chem. Phys., 4, 1885-1893, 10.5194/acp-4-1885-2004, 2004.
742 Sahu, L. K., Kondo, Y., Moteki, N., Takegawa, N., Zhao, Y., Cubison, M. J., Jimenez, J. L., Vay, S.,
743 Diskin, G. S., Wisthaler, A., Mikoviny, T., Huey, L. G., Weinheimer, A. J., and Knapp, D. J.:
744 Emission characteristics of black carbon in anthropogenic and biomass burning plumes
745 over California during ARCTAS-CARB 2008, Journal of Geophysical Research-Atmospheres,
746 117, 10.1029/2011jd017401, 2012.
747 Schnaiter, M., Linke, C., Mohler, O., Naumann, K. H., Saathoff, H., Wagner, R., Schurath, U., and
748 Wehner, B.: Absorption amplification of black carbon internally mixed with secondary
749 organic aerosol, Journal of Geophysical Research-Atmospheres, 110,
750 10.1029/2005jd006046, 2005.
751 Schwarz, J. P., Gao, R. S., Fahey, D. W., Thomson, D. S., Watts, L. A., Wilson, J. C., Reeves, J. M.,
752 Darbeheshti, M., Baumgardner, D. G., Kok, G. L., Chung, S. H., Schulz, M., Hendricks, J., Lauer,
753 A., Karcher, B., Slowik, J. G., Rosenlof, K. H., Thompson, T. L., Langford, A. O., Loewenstein, M.,
754 and Aikin, K. C.: Single-particle measurements of midlatitude black carbon and
755 light-scattering aerosols from the boundary layer to the lower stratosphere, Journal of
756 Geophysical Research-Atmospheres, 111, 10.1029/2006jd007076, 2006.
757 Schwarz, J. P., Gao, R. S., Spackman, J. R., Watts, L. A., Thomson, D. S., Fahey, D. W., Ryerson, T.
758 B., Peischl, J., Holloway, J. S., Trainer, M., Frost, G. J., Baynard, T., Lack, D. A., de Gouw, J. A.,
759 Warneke, C., and Del Negro, L. A.: Measurement of the mixing state, mass, and optical size of

760 individual black carbon particles in urban and biomass burning emissions, Geophysical
761 Research Letters, 35, 10.1029/2008gl033968, 2008.
762 Schwarz, J. P., Spackman, J. R., Gao, R. S., Perring, A. E., Cross, E., Onasch, T. B., Ahern, A.,
763 Wrobel, W., Davidovits, P., Olfert, J., Dubey, M. K., Mazzoleni, C., and Fahey, D. W.: The
764 Detection Efficiency of the Single Particle Soot Photometer, Aerosol Sci. Technol., 44,
765 612-628, 10.1080/02786826.2010.481298, 2010.
766 Seinfeld, J. H., and Pandis, S. N.: Atmospheric chemistry and physics: from air pollution to
767 climate change, John Wiley & Sons, 2012.
768 Shiraiwa, M., Kondo, Y., Iwamoto, T., and Kita, K.: Amplification of light absorption of black
769 carbon by organic coating, Aerosol Sci. Technol., 44, 46-54, 10.1080/02786820903357686,
770 2010.
771 Song, X. H., Hopke, P. K., Fergenson, D. P., and Prather, K. A.: Classification of single particles
772 analyzed by ATOFMS using an artificial neural network, ART-2A, Analytical Chemistry, 71,
773 860-865, 10.1021/ac9809682, 1999.
774 Soto-Garcia, L. L., Andreae, M. O., Andreae, T. W., Artaxo, P., Maenhaut, W., Kirchstetter, T.,
775 Novakov, T., Chow, J. C., and Mayol-Bracero, O. L.: Evaluation of the carbon content of
776 aerosols from the burning of biomass in the Brazilian Amazon using thermal, optical and
777 thermal-optical analysis methods, Atmospheric Chemistry and Physics, 11, 4425-4444,
778 2011.
779 Stephens, M., Turner, N., and Sandberg, J.: Particle identification by laser-induced
780 incandescence in a solid-state laser cavity, Appl. Optics, 42, 3726-3736,
781 10.1364/ao.42.003726, 2003.
782 Takahama, S., Russell, L. M., Shores, C. A., Marr, L. C., Zheng, J., Levy, M., Zhang, R., Castillo, E.,
783 Rodriguez-Ventura, J. G., Quintana, P. J. E., Subramanian, R., Zavala, M., and Molina, L. T.:
784 Diesel vehicle and urban burning contributions to black carbon concentrations and size
785 distributions in Tijuana, Mexico, during the Cal-Mex 2010 campaign, Atmos. Environ., 88,
786 341-352, 10.1016/j.atmosenv.2013.09.057, 2014.
787 Taylor, J. W., Allan, J. D., Liu, D., Flynn, M., Weber, R., Zhang, X., Lefer, B. L., Grossberg, N.,
788 Flynn, J., and Coe, H.: Assessment of the sensitivity of core/shell parameters derived using
789 the single-particle soot photometer to density and refractive index, Atmos. Meas. Tech.

Discuss., 7, 5491-5532, 10.5194/amtd-7-5491-2014, 2014.

Wang, Q., Zhuang, G., Huang, K., Liu, T., Deng, C., Xu, J., Lin, Y., Guo, Z., Chen, Y., Fu, Q., Fu, J. S., and Chen, J.: Probing the severe haze pollution in three typical regions of China: Characteristics, sources and regional impacts, Atmos. Environ., 120, 76-88, http://dx.doi.org/10.1016/j.atmosenv.2015.08.076, 2015.

Wang, X., Ye, X., Chen, H., Chen, J., Yang, X., and Gross, D. S.: Online hygroscopicity and chemical measurement of urban aerosol in Shanghai, China, Atmos. Environ., 95, 318-326, http://dx.doi.org/10.1016/j.atmosenv.2014.06.051, 2014.

Willis, M. D., Healy, R. M., Riemer, N., West, M., Wang, J. M., Jeong, C. H., Wenger, J. C., Evans, G. J., Abbatt, J. P. D., and Lee, A. K. Y.: Quantification of black carbon mixing state from traffic: implications for aerosol optical properties, Atmos. Chem. Phys. Discuss., 15, 33555-33582, 10.5194/acpd-15-33555-2015, 2015.

Yao, X., Chan, C. K., Fang, M., Cadle, S., Chan, T., Mulawa, P., He, K., and Ye, B.: The water-soluble ionic composition of PM2.5 in Shanghai and Beijing, China, Atmos. Environ., 36, 4223-4234, http://dx.doi.org/10.1016/S1352-2310(02)00342-4, 2002.

Zhang, G., Bi, X., He, J., Chen, D., Chan, L. Y., Xie, G., Wang, X., Sheng, G., Fu, J., and Zhou, Z.: Variation of secondary coatings associated with elemental carbon by single particle analysis, Atmos. Environ., 92, 162-170, http://dx.doi.org/10.1016/j.atmosenv.2014.04.018, 2014.

Zhang, R., Khalizov, A. F., Pagels, J., Zhang, D., Xue, H., and McMurry, P. H.: Variability in morphology, hygroscopicity, and optical properties of soot aerosols during atmospheric processing, Proceedings of the National Academy of Sciences, 105, 10291-10296, 10.1073/pnas.0804860105, 2008.

Zhang, Y. X., Zhang, Q., Cheng, Y. F., Su, H., Kecorius, S., Wang, Z. B., Wu, Z. J., Hu, M., Zhu, T., Wiedensohler, A., and He, K. B.: Measuring morphology and density of internally mixed black carbon with SP2 and VTDMA: new insight to absorption enhancement of black carbon in the atmosphere, Atmos. Meas. Tech. Discuss., 2015, 12025-12050, 10.5194/amtd-8-12025-2015, 2015.

819 **Table 1.** Names, numbers and fractions of the six types of BC-containing particles
820 detected by the SPAMS instrument.

| Group | Number of particles | Fraction of particles |
|---|---|---|
| Pure BC | 535 | 0.62% |
| Biomass Burning BC-containing (BBBC) | 22 007 | 25.57% |
| K-rich BC-containing (KBC) | 11 343 | 13.18% |
| BC internally-mixed with OC and ammonium nitrate (BCOC-NOx) | 33 760 | 39.23% |
| BC internally-mixed with OC and ammonium sulfate (BCOC-SOx) | 15 291 | 17.77% |
| Unidentified | 3121 | 3.63% |
| Total BC-containing | 86 057 | 100% |

821
822

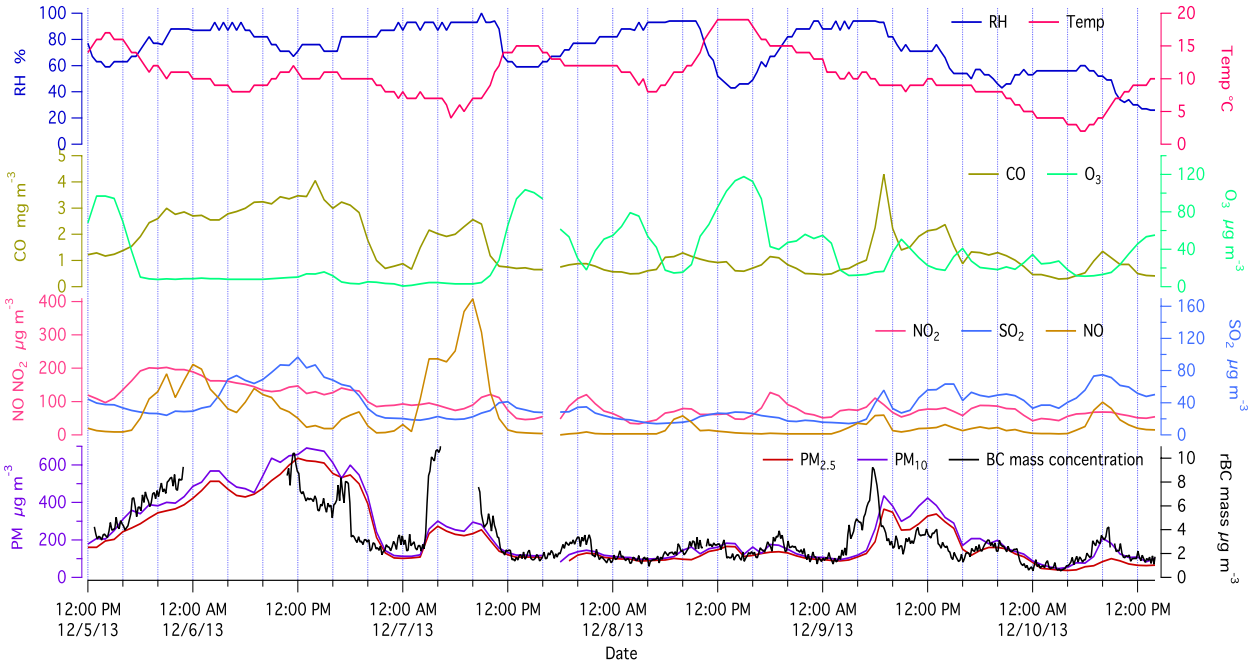


**Figure 1.** Temporal profiles of temperature and relative humidity with 30 min resolution, gaseous pollutants (CO, $O_3$, $SO_2$, NO and $NO_2$) with 60 min resolution, and $PM_{2.5}$ and $PM_{10}$ mass concentrations with 60 min resolution. The concentration of rBC mass (black trace in the bottom panel, 10 min resolution) was continuously measured by SP2.

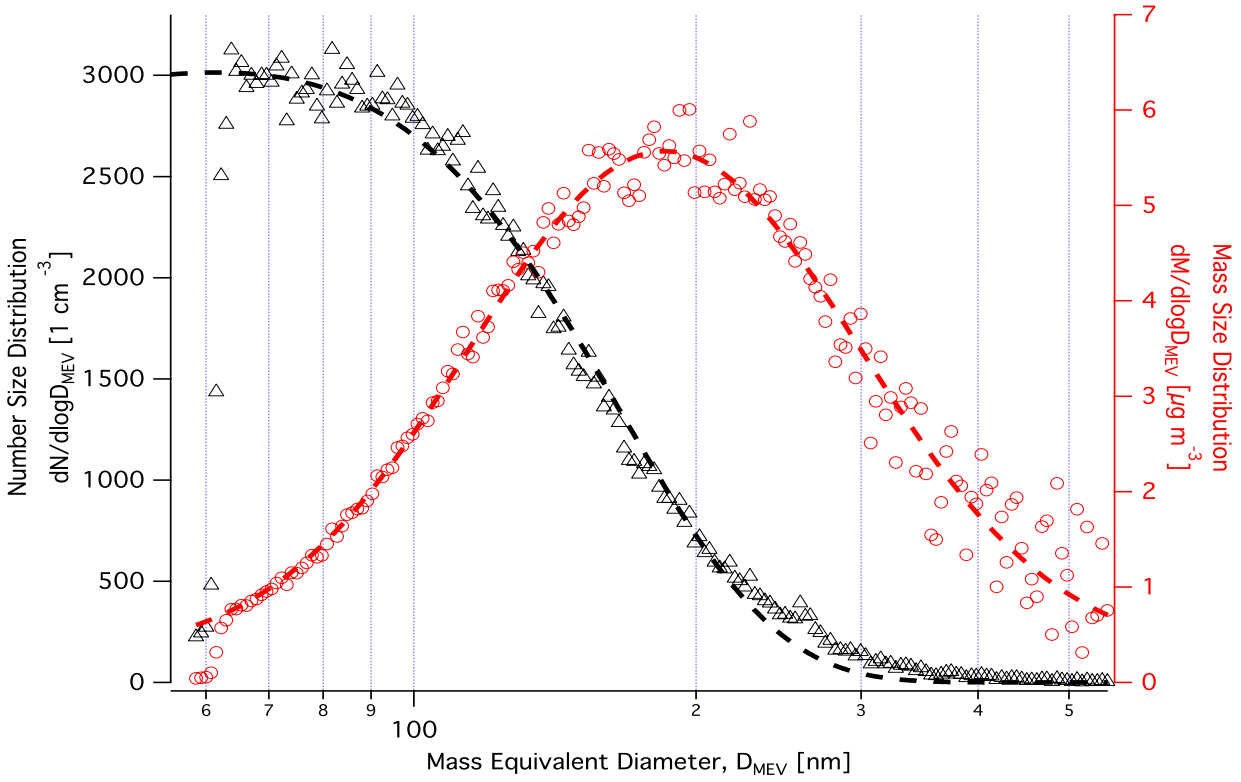


831

832 **Figure 2.** The measured rBC core mass size distribution and number size distribution are
833 shown in open red circles and black triangles, respectively. The log-normal fits to the
834 observed distributions are shown by the dashed lines.

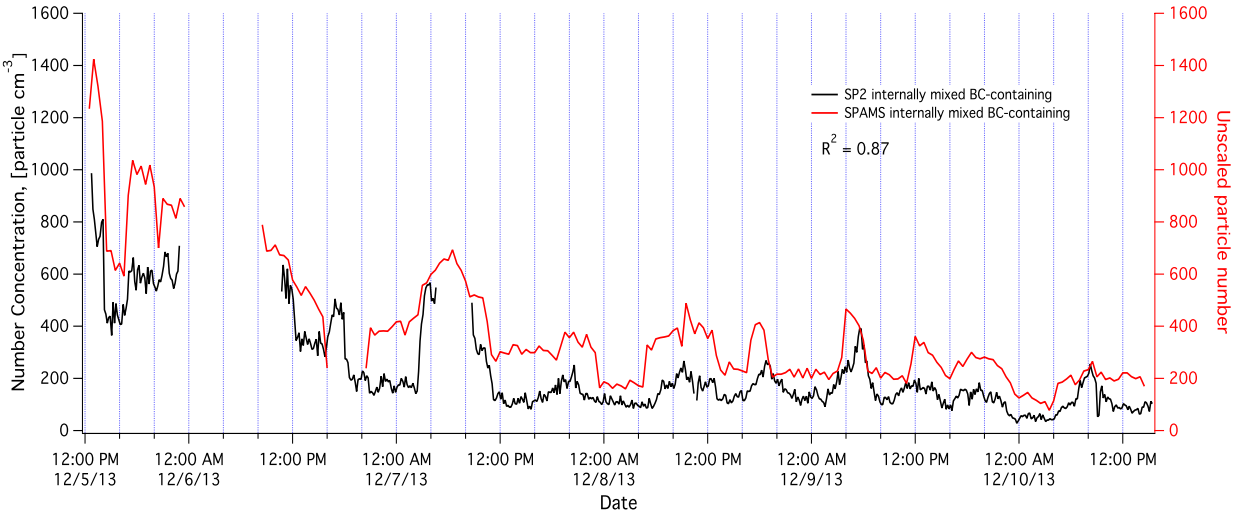


835

836 **Figure 3.** Comparison of the SPMAS-detected internally-mixed BC-containing particles and
837 SP2-detected internally-mixed rBC-containing particles.

838

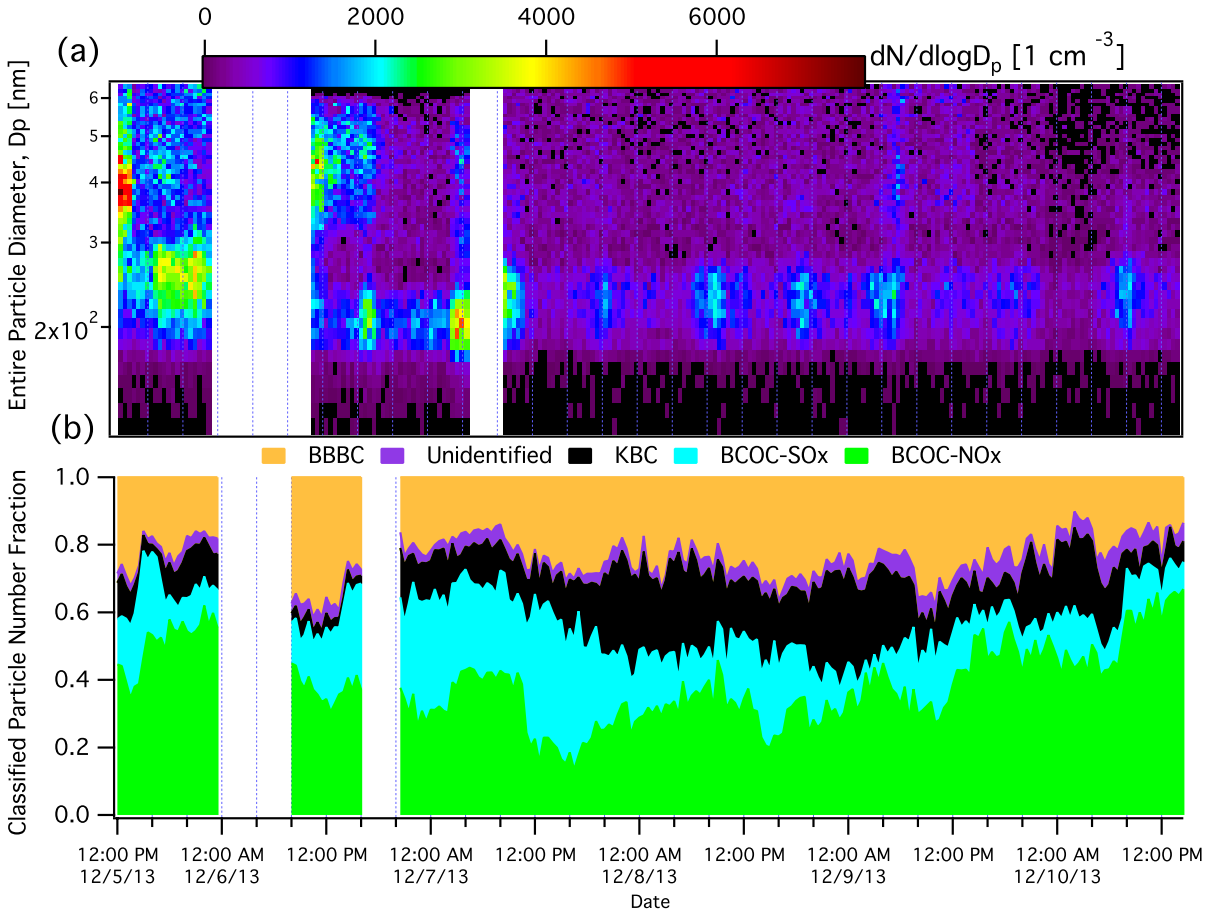


839

840 **Figure 4.** (a) Temporal variations of number and size distributions for rBC-containing
841 particles detected by SP2 with 30 min resolution. (b) Temporal variation of number
842 fractions of different BC-containing particle types with 10 min time resolution (detected
843 by SPAMS).

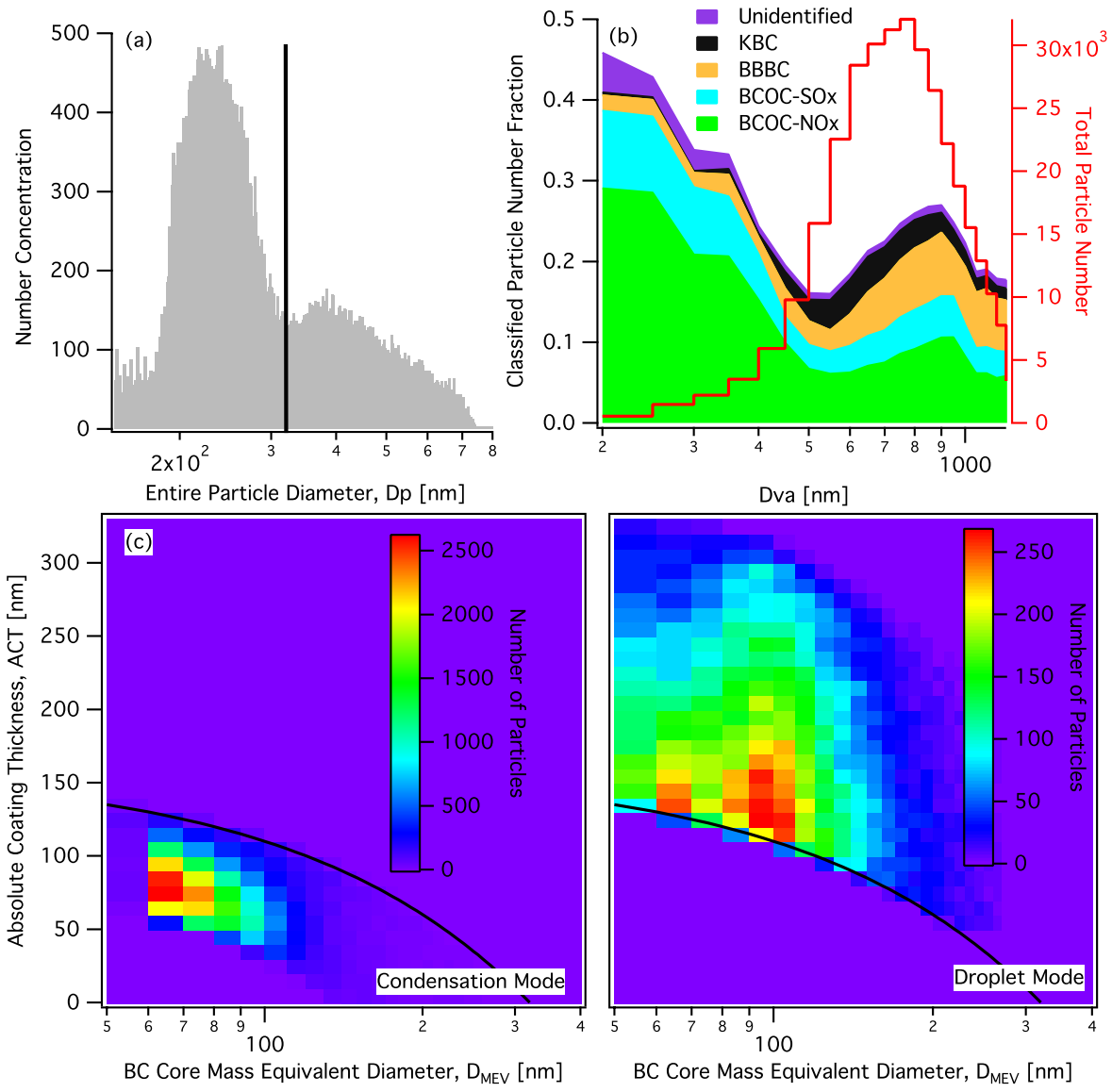


**Figure 5. (a)** $D_p$ number size distribution histogram for the SP2-detected rBC-containing particles. **(b)** $D_{va}$ number fraction distribution of SPAMS-detected BC-containing particles color-coded by the particle type. **(c)** $D_c$ and ACT with number size distribution in the condensation and droplet modes.

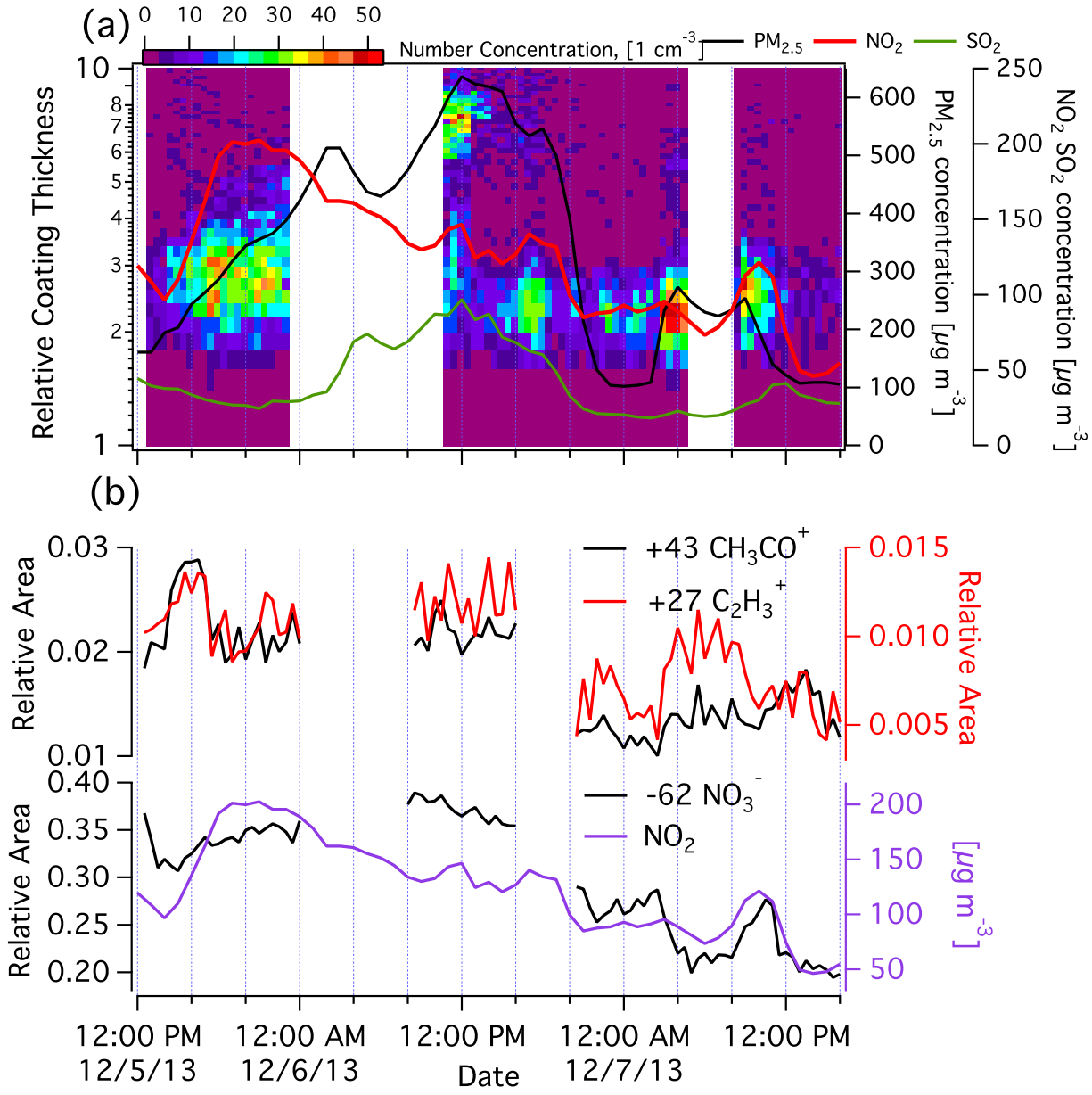


849

850 **Figure 6.** (a) Temporal variation of the relative coating thickness distribution of
851 traffic-emitted rBC-containing particles (SP2) with resolutions of 0.2 RCT and 30 min
852 and the temporal profile of $NO_2$ and $PM_{2.5}$ concentrations with 60 min resolution. (b)
853 Temporal variation of relative peak areas of +27 ($C_2H_3^+$), +43 ($CH_3CO^+$) and -62 ($NO_3^-$)
854 of traffic-emitted BC-containing particles (SPAMS) and $NO_2$ concentration with 30 min
855 resolution.